

Diverse Gaussian Noise Consistency Regularization for Robustness and Uncertainty Calibration under Noise Domain Shifts

Athanasios Tsiligkaridis^{*†}, Theodoros Tsiligkaridis^{*‡}

[†]Department of Electrical and Computer Engineering, Boston University, Boston, MA, USA

[‡]Artificial Intelligence Technology Group, MIT Lincoln Laboratory, Lexington, MA USA

[†]atsili@bu.edu, [‡]ttsili@mit.edu

Abstract

Deep neural networks achieve high prediction accuracy when the train and test distributions coincide. In practice though, various types of corruptions occur which deviate from this setup and cause severe performance degradations. Few methods have been proposed to address generalization in the presence of unforeseen domain shifts. In particular, digital noise corruptions arise commonly in practice during the image acquisition stage and present a significant challenge for current robustness approaches. In this paper, we propose a diverse Gaussian noise consistency regularization method for improving robustness of image classifiers under a variety of noise corruptions while still maintaining high clean accuracy. We derive bounds to motivate our Gaussian noise consistency regularization using a local loss landscape analysis. We show that this simple approach improves robustness against various unforeseen noise corruptions over standard and adversarial training and other strong baselines. Furthermore, when combined with diverse data augmentation techniques we empirically show this type of consistency regularization further improves robustness and uncertainty calibration for common corruptions upon the state-of-the-art for several image classification benchmarks.

1 Introduction

Deep neural networks are increasingly being used in computer vision and have achieved state-of-the-art performance on image classification [Krizhevsky et al., 2012, He et al., 2015, Huang et al., 2019]. However, when the test distribution differs from the train distribution, performance can suffer as a result, even for mild image corruptions and transformations [Hendrycks and Dietterich, 2019]. In fact, models have unrealistic behavior when faced with out-of-distribution inputs that arise from synthetic corruptions [Hendrycks and Dietterich, 2019], spatial transformations [Engstrom et al., 2019], and data collection setups [Torralba and Efros, 2011, Recht et al., 2019]. Although train/test distribution mismatch is common in

practice, the problem has not been thoroughly studied. Designing models that provide robustness to unforeseen deviations from the train distribution is highly desirable. Furthermore, calibrated uncertainty on test sets associated with a domain shift is also desirable as models can know when mistakes are likely to be made, improving human-machine teaming.

The majority of the literature on robustness has focused on adversarial robustness against pixel-level ℓ_p norm-bounded perturbations [Madry et al., 2018, Zhang et al., 2019]. However, the ℓ_p norm-bounded perturbation model for corruptions does not account for common corruptions, such as rotation, translation, blur, and contrast changes, that are often encountered in practice. Semantic perturbations that alter image attributes while maintaining a natural look have been also shown to fool classifiers [Joshi et al., 2019, Xiao et al., 2021]. Such domain shifts often correspond to large ℓ_p perturbations that circumvent defenses against imperceptible pixel-level perturbations. Sampling the entire space of possible image variations is not practical to protect models against test time failures, and knowledge of the test distribution is not warranted.

The natural approach to defending against a particular fixed distribution shift is to explicitly incorporate such data into the training process [Kang et al., 2019]. However, this paradigm has drawbacks including over-fitting to one type of corruption [Geirhos et al., 2018]; in [Kang et al., 2019], it was shown that ℓ_∞ robustness provides poor generalization to unforeseen attacks. The empirical study in [Chun et al., 2019] shows that several expensive methods improve robustness at the cost of lower clean accuracy or degraded uncertainty estimation and there are large trade-offs for various regularization methods. Data augmentation policies have been proposed to increase clean accuracy [Cubuk et al., 2019] based on reinforcement learning but are computationally expensive. Uncertainty calibration can be improved by simple ensembles [Lakshminarayanan et al., 2017] and pre-training [Hendrycks et al., 2019]. However, it has been shown that calibration degrades significantly under domain shifts [Ovadia et al., 2019].

Recent work [Hendrycks et al., 2020, 2021] proposed diverse data augmentations to improve robustness and uncertainty calibration against common corruptions. However, robustness to noise corruptions remains a challenge. Digital noise corruptions occur often in real world scenarios due to imaging sensors and/or other devices hardware imperfections, and environmental conditions [Gonzalez and Woods, 2018,

^{*}Equal contribution.

Awad, 2019]. The gaps between clean accuracy/uncertainty and accuracy/uncertainty under noise domain shifts are still large; it remains an open question how to close these gaps.

In this work, we propose a training technique that enforces consistency between clean and noisy examples at different scales to enhance robustness against unforeseen digital noise corruptions. Our approach can be characterized as a type of Gaussian data augmentation strategy coupled with consistency regularization. Another way to interpret our approach is through the lens of local loss landscape regularity as our proposed consistency regularization method induces both a smoothing (curvature minimization) and flattening (gradient norm minimization) effect on the local loss landscape. Our experimental results show that our method produces models that improve robustness in the presence of various practical unforeseen noise distribution shifts. Furthermore, the combination of our approach with diverse data augmentations achieves state-of-the-art (SOTA) robustness and uncertainty calibration against common corruptions.

Our contributions are summarized below:

- We introduce a consistency loss based on the Kullback-Leibler (KL) divergence that embeds clean examples similarly to diverse Gaussian noise augmentations, and a corresponding training algorithm (DiGN).
- We provide an analysis of our Gaussian noise consistency loss that uncovers an inducing effect of smoothing (minimizing curvature) and flattening of the local loss landscape.
- We experimentally show our approach outperforms several competitive baselines against various unforeseen noise corruptions on CIFAR-10-C, CIFAR-100-C, and Tiny-ImageNet-C dataset. Additionally, we show our approach can be effectively combined with diverse data augmentation methods to achieve SOTA robustness and uncertainty calibration against all common corruptions.

2 Background and Related Work

We assume labeled data of the form $(x, y) \sim \mathcal{D}$ drawn from distribution \mathcal{D} . The labels y correspond to C classes. Neural network function $f_\theta(\cdot)$ maps inputs into logits, and θ are the model parameters. The softmax layer is used to map logits into class probability scores given by $p_c(x) = e^{f_{\theta,c}(x)} / \sum_i e^{f_{\theta,i}(x)}$.

Standard Training. The standard criterion for training deep neural networks is empirical risk minimization (Standard):

$$\min_{\theta} \mathbb{E}_{(x,y) \sim \mathcal{D}} [\mathcal{L}(f_\theta(x), y)] \quad (1)$$

where the loss is chosen to be the cross-entropy function $\mathcal{L}(f_\theta(x), y) = -y^T \log p_\theta(x)$. While training using the criterion (1) yields high accuracy on clean test sets, network generalization performance to various data shifts may suffer.

Adversarial Training against ℓ_p Adversary. Adversarial training (AT) [Madry et al., 2018] is one of the most effective defenses against ℓ_p norm-bounded perturbations which minimizes the adversarial risk,

$$\min_{\theta} \mathbb{E}_{(x,y) \sim \mathcal{D}} \left[\max_{\|\delta\|_p \leq \epsilon} \mathcal{L}(f_\theta(x + \delta), y) \right] \quad (2)$$

During the training process, adversarial attacks are computed at inputs x that solve the inner maximization problem. The inner maximization may be solved iteratively using projected gradient descent (PGD) for norms $p \in \{2, \infty\}$, i.e., $\delta^{(k+1)} = \mathcal{P}_{B_p(\epsilon)}(\delta^{(k)} + \alpha \nabla_{\delta} \mathcal{L}(x + \delta^{(k)}, y))$ where $\mathcal{P}_{B_p(\epsilon)}(z) = \arg \min_{u \in B_p(\epsilon)} \|z - u\|_2^2$ is the orthogonal projection onto the constraint set. Another robust training approach that trades-off the natural and robust error using smoothing is TRADES [Zhang et al., 2019]:

$$\min_{\theta} \mathbb{E}_{(x,y) \sim \mathcal{D}} \left[\mathcal{L}(f_\theta(x), y) + \lambda \max_{\|p\|_p \leq \epsilon} D(p(x; \theta) \| p(x + \delta; \theta)) \right] \quad (3)$$

where D denotes the Kullback-Leibler divergence $D(p \| q) = \sum_c p_c \log \frac{p_c}{q_c}$ and the inner maximization is computed using PGD.

These robust methods optimize robustness only inside the ϵ -ball of the training distribution which does not capture *perceptible* data shifts such as common image corruptions [Hendrycks and Dietterich, 2019]. Training with arbitrarily large ϵ in the pixel-wise robustness formulations fails in practice as image quality degrades and clean accuracy suffers due to inherent tradeoff [Tsipras et al., 2019].

Random Self-Ensemble Training. In the context of adversarial robustness, a random self-ensemble (RSE) method has been proposed [Liu et al., 2018] based on noise injection at the input layer and each layer of neural networks and was demonstrated to provide good levels of robustness against white-box attacks. Considering noise at the input layer only, the RSE training criterion is:

$$\min_{\theta} \mathbb{E}_{(x,y) \sim \mathcal{D}} \left[\mathbb{E}_{\delta \sim \mathcal{N}(0, \sigma^2 I)} \mathcal{L}(f_\theta(x + \delta), y) \right] \quad (4)$$

and predictions are ensembled at inference time as $\hat{y}(x) = \arg \max_c \frac{1}{n} \sum_{i=1}^n p_c(x + \delta_i)$ where $\delta_i \sim \mathcal{N}(0, \sigma^2 I)$. This increases inference time due to the ensemble, is prone to overfitting at a fixed noise level σ , and cannot handle certain real-world corruptions well, such as contrast and fog.

Diverse Data Augmentation Training. A recent data augmentation technique, AugMix [Hendrycks et al., 2020], was shown to achieve SOTA performance against unforeseen corruptions by enforcing a consistency loss coupled with a data augmentation scheme:

$$\min_{\theta} \mathbb{E}_{(x,y) \sim \mathcal{D}} \left[\mathcal{L}(f_\theta(x), y) + \lambda JS(p_\theta(x); p_\theta(x_{a,1}); p_\theta(x_{a,2})) \right] \quad (5)$$

where $JS(p_1; p_2; p_3) = \frac{1}{3}(D(p_1 \| p_{\text{mix}}) + D(p_2 \| p_{\text{mix}}) + D(p_3 \| p_{\text{mix}}))$ is the Jensen-Shannon divergence, $p_{\text{mix}} = \frac{1}{3}(p_1 + p_2 + p_3)$, and $x_{a,1}, x_{a,2}$ are augmented variants of x formed by mixing composition chains each consisting of a finite number of augmentation operations chosen from the set {rotate, posterize, shear-x, shear-y, translate-x, translate-y, solarize, equalize, autocontrast}. Using diversity and randomness in choosing these operations and mixing weights at different levels of severity during training, this data augmentation method is empirically shown to significantly improve robustness against unforeseen corruptions in comparison to CutOut [DeVries and Taylor, 2017], MixUp [Zhang et al., 2017, Tokozume et al., 2018], CutMix [Yun

et al., 2019], and AutoAugment [Cubuk et al., 2018] schemes.

Another data augmentation technique shown to improve strong performance against such corruptions is DeepAugment [Hendrycks et al., 2021], which distorts images by perturbing internal representations of image-to-image networks. These perturbations include zeroing, negating, convolving, transposing, applying activation functions, etc. and generate semantically similar images for training.

While these baseline offer good performance, they still have difficulty dealing with certain noise and blur-based corruptions which can be further improved upon. We show that our Gaussian noise consistency regularization approach outperforms these methods under noise domain shifts, and when it is combined with diverse data augmentations, it achieves near SOTA performance against unforeseen common corruptions.

3 Diverse Gaussian Noise Consistency Regularization

Our primary goal is to design a training method to improve generalization against a variety of noise corruptions while fitting in existing pipelines with minimal changes. We introduce a consistency loss that embeds representations of clean examples, x , and noisy examples, $x + \delta$, similarly. To increase resiliency against a variety of noise distributions, we diversify the perturbation statistics by choosing a random noise level σ uniformly in the range $[0, \sigma_{\max}]$ and then generating the random perturbation $\delta \sim \mathcal{N}(0, \sigma^2 I)$.

Our proposed training criterion is:

$$\min_{\theta} \mathbb{E}_{(x,y) \sim \mathcal{D}} \left[\mathcal{L}(f_{\theta}(x), y) + \lambda \mathbb{E}_{\sigma \sim \mathcal{U}([0, \sigma_{\max}])} \mathbb{E}_{\delta \sim \mathcal{N}(0, \sigma^2 I)} D(p_{\theta}(x) \parallel p_{\theta}(x + \delta)) \right] \quad (6)$$

The classification loss $\mathcal{L}(f_{\theta}(x), y)$ in (6) maximizes accuracy on clean examples, while the consistency regularization terms force clean and noisy examples to have similar output distributions. Here, $\lambda \geq 0$ is a regularization parameter, \mathcal{U} denotes uniform distribution, $\mathcal{N}(0, \sigma^2 I)$ denotes the normal distribution with standard deviation σ .

We call our approach (6) Diverse Gaussian Noise consistency regularization, DiGN, and Algorithm 1 depicts our training procedure. A sample-based approximation is used to approximate the regularizer to maintain low computational complexity during training. In practice, a couple samples suffice to obtain strong robustness and uncertainty calibration. The concept is graphically illustrated in Figure 1.

The motivation for placing distributions on scale parameters σ and associated noise perturbations δ to approximate (6) is to avoid memorization of fixed scale augmentations [Geirhos et al., 2018] which leads to poor generalization against various noise domain shifts. In contrast to RSE (4) which uses a fixed scale jointly with test-time ensembling at the same scale, we use a diverse set of Gaussian noise scales and do not rely on test-time ensembling. In contrast to AugMix (5), DiGN only makes use of Gaussian noise augmentations, and leverages the Kullback-Leibler divergence instead of the Jensen-Shannon divergence as the consistency loss.

Interestingly, training with diverse Gaussian noise augmentations provides robustness not only against Gaussian noise,

Algorithm 1 DiGN pseudocode

Input: Training data $\{(x_i, y_i)\}$, Network f_{θ} , Training epochs T , Batch size $|B|$, learning rate schedule η_t , hyperparameters $(\lambda, \sigma_{\max}, n)$
Result: Trained network f_{θ}
for $t=0$ to $T-1$ **do**
 for each batch $(x, y) \sim \mathcal{D}$ **do**
 for sample $k \in \{1, \dots, n\}$ **do**
 Generate $\sigma^{(k)} \sim \mathcal{U}(0, \sigma_{\max})$ for each example
 Generate $\delta^{(k)} \sim \mathcal{N}(0, (\sigma^{(k)})^2 I)$ for each example
 $x_{\delta}^{(k)} = x + \delta^{(k)}$
 end for
 $R(x_i) = \frac{1}{n} \sum_{k=1}^n D(p_{\theta}(x_i) \parallel p_{\theta}(x_{i, \delta}^{(k)}))$
 $\mathcal{L}_T(x_i, y_i) = \mathcal{L}(x_i, y_i) + \lambda R(x_i)$
 $\theta = \theta - \eta_t \frac{1}{|B|} \sum_{i \in B} \nabla_{\theta} \mathcal{L}_T(x_i, y_i)$
 end for
end for

but also against a variety of weather, blur, noise and digital corruptions, as evidenced in our results.

3.1 Analysis of Gaussian Noise Consistency Regularization

In this section, we analyze the effect of Gaussian noise consistency regularization in the small-noise regime. Specifically, we obtain a relationship between loss curvature and Fisher information which is further used to derive a bound on the local loss deviation in a neighborhood of data examples. This bound aids in understanding the effect of Gaussian noise consistency regularization on the local loss landscape.

Using a second-order Taylor expansion on the KL divergence, for small σ [Kullback, 1997]:

$$D(p_{\theta}(x) \parallel p_{\theta}(x + \delta)) \approx \frac{1}{2} \delta^T G_{\theta}(x) \delta$$

where $G_{\theta}(x)$ is the Fisher information matrix (FIM) given by:

$$G_{\theta}(x) = \sum_k [p_{\theta}(x)]_k \nabla_x \log[p_{\theta}(x)]_k (\nabla_x \log[p_{\theta}(x)]_k)^T \quad (7)$$

Taking the expectation,

$$\mathbb{E}_{\delta \sim \mathcal{N}(0, \sigma^2 I)} D(p_{\theta}(x) \parallel p_{\theta}(x + \delta)) = \frac{\sigma^2}{2} \text{Tr}(G_{\theta}(x)) \quad (8)$$

where we used $\mathbb{E}_{\delta \sim \mathcal{N}(0, \sigma^2 I)} [\delta \delta^T] = \sigma^2 I$. Taking the outer expectation wrt. σ on approximation (8):

$$\begin{aligned} & \mathbb{E}_{\sigma \sim \mathcal{U}([0, \sigma_{\max}])} \mathbb{E}_{\delta \sim \mathcal{N}(0, \sigma^2 I)} D(p_{\theta}(x) \parallel p_{\theta}(x + \delta)) \\ & \approx \mathbb{E}_{\sigma \sim \mathcal{U}([0, \sigma_{\max}])} \left[\frac{\sigma^2}{2} \right] \text{Tr}(G_{\theta}(x)) = \frac{\sigma_{\max}^2}{6} \text{Tr}(G_{\theta}(x)) \quad (9) \end{aligned}$$

The FIM has a strong connection to curvature; in fact for the case of cross-entropy, the Hessian matrix of the loss function is identical to the FIM (7), as the next proposition shows.

Proposition 1. *The following relation holds $H(x) := \nabla_x^2 \mathcal{L}(f_{\theta}(x), y) = G_{\theta}(x)$.*

Thus, minimizing with the Gaussian noise regularizer (9) is

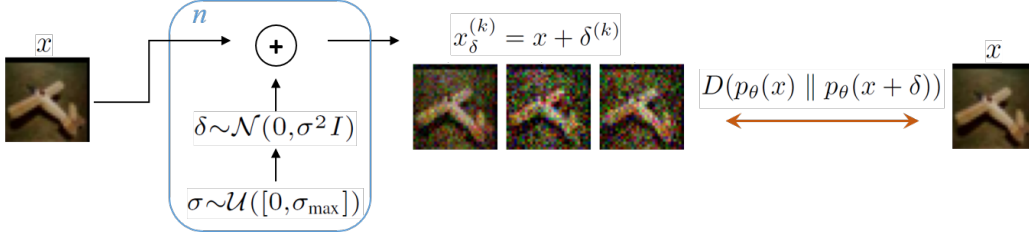


Figure 1: An illustration of our DiGN training methodology. During training, input images x are fed into n independent branches each associated with a new augmented sample. Each branch adds Gaussian noise δ to clean images controlled by a variety of scales σ sampled from a uniform distribution, and a consistency loss with respect to the clean images is formed.

equivalent to minimizing the curvature in all directions equally since $\text{Tr}(H(x)) = \sum_i \lambda_i(H(x))$, where λ_i denotes the sorted Hessian eigenvalues. This has the effect of inducing low curvature in the loss landscape of \mathcal{L} around x and encourages locally linear behavior.

What we show next is that there is another interesting effect that the KL smoothing regularizer induces. Substituting (7) into (9) and simplifying, we obtain:

$$\begin{aligned} \mathbb{E}_{\sigma \sim \mathcal{U}([0, \sigma_{\max}])} \mathbb{E}_{\delta \sim \mathcal{N}(0, \sigma^2)} D(p_{\theta}(x) \parallel p_{\theta}(x + \delta)) \\ \approx \frac{\sigma_{\max}^2}{6} \sum_k [p_{\theta}(x)]_k \|\nabla_x \log[p_{\theta}(x)]_k\|_2^2 \quad (10) \end{aligned}$$

This can be interpreted a regularization term that induces stability of predictions within a local neighborhood of x through weighted logit smoothing. This type of weighted logit smoothing leads to a bound on the local loss deviation.

Theorem 1. *The following bound holds on the loss function:*

$$\begin{aligned} |\mathcal{L}(x + \delta, y) - \mathcal{L}(x, y)| \leq \|\delta\|_2 \cdot \sqrt{\sum_k y_k \|\nabla_x \log p(x)_k\|_2^2} \\ + \frac{1}{2} \lambda_{\max}(H(x)) \|\delta\|_2^2 + o(\|\delta\|_2^2) \quad (11) \end{aligned}$$

A consequence of Theorem 1 is that for correct classifications where $y_k \approx p(x)_k$, minimizing the regularizer (10) has a twofold effect: (a) curvature is minimized, as the Hessian trace upper bounds the maximum Hessian eigenvalue of the loss $\mathcal{L}(x, y)$, $\lambda_{\max}(H(x)) \leq \text{Tr}(H(x))$, and (b) loss surface flatness is increased by minimizing the norm of the loss gradient, $\|\nabla_x \mathcal{L}(x, y)\|_2$. The joint effect of minimizing curvature and encouraging flatness in a neighborhood of x implies improved stability of the prediction as the loss changes are small with respect to small perturbations δ and as a result predictions are invariant to such perturbations.

4 Experimental Results

Datasets. The datasets used for our experimental results are (a) CIFAR-10, (b) CIFAR-100 [Krizhevsky et al., 2009], and (c) Tiny-ImageNet [Li et al., 2014]. The CIFAR-10/100 datasets contain color images of size $32 \times 32 \times 3$ spanned across 50,000 train images and 10,000 test images, while Tiny-ImageNet contains color images of size $64 \times 64 \times 3$ spanned across 100,000 train images and 10,000 test images. Robustness against data shifts is measured by evaluating on CIFAR-10-C, CIFAR-100-C, and Tiny-ImageNet-C

[Hendrycks and Dietterich, 2019]. Each CIFAR corrupted dataset contains a total of $M = 18$ corruptions at $J = 5$ severity levels. The Tiny-ImageNet corrupted dataset contains $M = 14$ corruptions at $J = 5$ severity levels. The ‘gaussian noise’ corruption is excluded from our evaluations for fairness.

Computing infrastructure. All experiments were performed using 2 Volta V100 GPUs and 4 CPU cores. Methods were all implemented using the PyTorch deep learning framework.

Baselines. The baseline methods considered include standard training (Standard), adversarial training (AT), tradeoff-inspired adversarial defense via surrogate-loss minimization (TRADES), random self-ensemble (RSE), diverse augmentation mixing chains (AugMix), deep augmentations (DeepAugment). The adversarial models based on AT and TRADES were trained against an ℓ_{∞} adversary. The DeepAugment model was trained using the Noise2Net approach in [Hendrycks et al., 2021] where randomly sampled image-to-image networks (composition of several randomized residual blocks using grouped convolutions) with random weights are used to generate deep image augmentations. We remark that AutoAugment is excluded from our comparisons because it was outperformed by a large margin by AugMix [Hendrycks et al., 2020].

Training Details. The DiGN training method is demonstrated on deep residual network architecture ResNet-18 [He et al., 2016], densely connected convolutional architecture DenseNet-121 [Huang et al., 2017] and Wide-ResNet-18. The learning rate is started at 0.1 and decays every 50 epochs by a factor of 10. Pre-processing steps include standard random cropping, random horizontal flips, color jitter (0.25) and random rotation (2 degrees).

Training was performed for 150 epochs using SGD with Nesterov momentum 0.9 and weight decay 0.0005. The model with the highest clean accuracy computed on the test set was selected as the best performer. For each performance metric, the mean and standard deviation accuracy over 3 independently trained model runs is reported.

The adversarial models based on AT and TRADES were trained using ℓ_{∞} norm-bounded constraints using $\epsilon = 8/255$ and 7 PGD steps with step size $2.5\epsilon/7$ to allow sufficient exploration of the constraint set’s boundary. For RSE, a noise standard deviation $\sigma = 0.1$ was chosen to achieve a high mCA experimentally with $n = 10$ samples used in test-time ensembling. For AugMix, $\lambda = 12$ was chosen as in the original implementation. For DiGN, we use the following hyperparameters based on experimentation: $\sigma_{\max} = 0.2, \lambda = 0.2$

for CIFAR-10, $\sigma_{\max} = 0.2$, $\lambda = 0.3$ for CIFAR-100, and $\sigma_{\max} = 0.6$, $\lambda = 0.2$ for Tiny-ImageNet. For DeepAugment, we used Noise2Net hyperparameters $\epsilon = 0.1$, and 2 hidden planes for CIFAR-10/100, $\epsilon = 0.2$ and 2 hidden planes for Tiny-ImageNet.

Performance Metrics. Classification performance on the clean dataset is measured using test accuracy, i.e., $\frac{1}{n} \sum_{i=1}^n \mathbb{1}_{\{y_i = \hat{y}_i\}}$. Robustness against domain shifts is measured using accuracy on a corrupted validation set for different severity levels j . For a specific corruption type $m \in \{1, \dots, M\}$ and severity level $j \in \{1, \dots, J\}$, let $A_{m,j}$ denote the corresponding accuracy. The *mean corruption accuracy (mCA)* is defined as: $mCA = \frac{1}{MJ} \sum_{m=1}^M \sum_{j=1}^J A_{m,j}$. We denote the mCA score computed over only noise corruptions as *mCA-N* (excluding Gaussian noise corruption for fairness).

Classifier calibration refers to the problem of true empirical correct likelihood matching the predicted confidence metric. This leads to trustworthy probability estimates of the model predictions. Uncertainty calibration performance is measured using the root-mean-square (RMS) calibration. Consider a partition of n_B bins $\{B_i\}$ that corresponding to increasing levels of confidence. Then, *RMS calibration error*, which measures the discrepancy between the empirical accuracy and the prediction confidence level $c_j = \max_c p_c(x_j)$, is computed as: $RMSE =$

$\sqrt{\sum_{i=1}^{n_B} \frac{|B_i|}{n} \left(\frac{1}{|B_i|} \sum_{j \in B_i} \mathbb{1}_{\{y_j = \hat{y}_j\}} - \frac{1}{|B_i|} \sum_{j \in B_i} c_j \right)^2}$. We denote the RMS calibration error computed only over noise corruptions as *RMSE-N* (excluding Gaussian noise).

Robustness Results. Classification accuracy results computed on the clean and noise-corrupted CIFAR-10, CIFAR-100, and Tiny-ImageNet test sets are shown in Table 1 for various deep learning methods on the ResNet-18 architecture. For CIFAR-10, our method DiGN outperforms Standard baseline by 33.7% mCA-N absolute improvement, and outperforms previous SOTA methods AugMix and DeepAugment by large margins 7.2% and 4.2%, adversarial training baselines AT and TRADES by 11.4% and 12.9%, and RSE by 5.2%. Similarly, for CIFAR-100, DiGN outperforms Standard and AugMix training by 40.2% and 13.9% in mCA-N, respectively. For Tiny-ImageNet, DiGN outperforms Standard and AugMix training by 16.0% and 9.1% in mCA-N, respectively. Overall, DiGN consistently achieves the best accuracy against unforeseen digital noise corruptions across all datasets, closing the gap between noise-corrupted and clean accuracies. Hyperparameters were experimentally chosen to achieve a high mCA-N score (see Supplementary Material for sensitivity analysis).

Next, we evaluate robustness against common corruptions. Classification accuracy results on clean and common corruptions are presented in Table 3 for CIFAR-10, CIFAR-100 and Tiny-ImageNet on ResNet-18. We observe that DiGN achieves high mCA scores improving upon Standard training by 8.6%, 11.0% and 3.0% for the CIFAR-10, CIFAR-100, and Tiny-ImageNet datasets respectively. In addition, the hybrid combination DiGN + AugMix¹ consistently achieves the high-

est mCA score improving upon the previous SOTA AugMix, implying that DiGN regularizes the model in a complementary way and improves generalization to a variety of digital noise corruptions that AugMix does not do so well on (see Table 1). We believe the reason for this is that AugMix tends to provide robustness against primarily low-frequency variations, while DiGN adds a complementary benefit to robustness by providing resilience against high-frequency variations.

Uncertainty Calibration Results. Calibration performance is measured in Table 2 on the clean and noise-corrupted validation sets on ResNet-18. DiGN offers significant improvements in RMSE calibration errors over Standard training; specifically, an average absolute improvement in RMSE calibration error of 24.8%, 25.1% and 13.4% on the noise subsets of CIFAR-10-C, CIFAR-100-C and Tiny-ImageNet-C validation sets, respectively. Furthermore, DiGN outperforms AugMix by 0.9%, 8.4% and 8.1% absolute RMSE calibration error improvement for noise subsets CIFAR-10-C, CIFAR-100-C and Tiny-ImageNet-C, respectively. Overall, DiGN offers substantial improvements in RMSE-N across all datasets and baseline methods while simultaneously achieving the SOTA in mCA-N robustness scores. Furthermore, the hybrid combination DiGN + AugMix shown in Table 3 achieves the lowest RMSE on all common corruptions.

Ablation Study. We perform an ablation study to measure the benefit of consistency regularization (CR) in the DiGN objective (6). We compare against training with diverse Gaussian noise augmentations directly denoted as DiGNw.o.CR training:

$$\min_{\theta} \mathbb{E}_{(x,y) \sim \mathcal{D}} \left[\mathbb{E}_{\sigma \sim \mathcal{U}([0, \sigma_{\max}])} \mathbb{E}_{\delta \sim \mathcal{N}(0, \sigma^2 I)} \mathcal{L}(f_{\theta}(x + \delta), y) \right] \quad (12)$$

Tables 1 and 2 show the superiority of the consistency-regularized DiGN over the DiGNw.o.CR baseline (12) for both robustness and calibration metrics.

Generalization to other network architectures. Robustness results on digital noise and all common corruptions are shown in Table 4 for the DenseNet-121 and Wide-ResNet-18 architectures. Our method DiGN continues to improve upon prior SOTA AugMix with margins ranging 9.3 – 14.0% in mCA-N. The hybrid combination DiGN + AugMix outperforms AugMix by margins ranging 2.1 – 3.7% in mCA. Calibration results are included in the Supplementary Material.

5 Limitations

Our focus in this work is designing deep image classifiers that are robust to digital noise corruptions at different levels of severity, while also improving performance to all common corruptions when our method is combined with other more generic data augmentation methods such as [Hendrycks et al., 2020]. While this work improves upon the SOTA in noise and all common corruptions, it remains to develop a more unified framework that encompasses all corruptions and more complex distribution shifts.

6 Conclusion

In this paper, a regularization method for training robust deep learning classifiers is presented based on diverse Gaussian noise augmentation at different scales coupled with consistency regularization. We empirically show that our training

¹This combination is implemented by combining the regularizers from (5) and (6) into the training loss.

	Standard	AT	TRADES	RSE	DeepAugment	AugMix	DiGNw.o.CR	DiGN
CIFAR-10								
Clean acc.	94.3±0.1	85.8±0.2	83.8±0.1	90.4±0.1	93.0±0.2	94.9±0.2	91.6±0.2	93.6±0.1
mCA-N	57.3±1.5	79.6±0.8	78.1±0.2	85.8±0.3	86.8±0.3	83.8±0.3	90.0±0.2	91.0±0.1
Gaussian Noise*	48.1±1.6	80.5±0.8	79.0±0.2	87.4±0.3	87.1±0.4	80.2±0.4	90.1±0.2	91.1±0.1
Impulse Noise	57.1±2.0	75.6±0.7	74.1±0.4	80.2±0.4	82.8±0.2	84.6±0.2	89.1±0.1	89.4±0.2
Shot Noise	60.3±1.2	81.4±0.8	79.9±0.2	88.0±0.3	88.7±0.4	84.9±0.4	90.3±0.2	91.7±0.2
Speckle Noise	63.6±1.2	80.9±0.9	79.5±0.2	87.5±0.4	88.7±0.3	85.6±0.3	90.4±0.2	91.7±0.1
CIFAR-100								
Clean acc.	75.8±0.1	59.5±0.4	61.4±0.2	66.7±0.2	71.9±0.1	76.4±0.1	67.8±0.2	72.8±0.1
mCA-N	28.3±0.5	48.0±0.9	51.4±0.7	58.8±0.7	58.2±0.5	54.6±0.9	65.4±0.1	68.5±0.1
Gaussian Noise*	21.4±0.6	51.1±0.8	53.4±0.6	61.5±0.9	57.2±0.6	47.8±1.1	65.3±0.1	68.6±0.0
Impulse Noise	28.6±0.5	37.8±1.6	43.7±1.4	49.0±0.7	55.1±0.3	60.3±0.5	64.0±0.1	66.0±0.2
Shot Noise	30.8±0.7	52.3±0.8	55.0±0.6	62.9±0.7	60.4±0.6	54.8±1.0	66.2±0.1	69.7±0.1
Speckle Noise	32.3±0.6	50.8±1.0	53.6±0.7	61.7±0.7	59.9±0.5	55.8±1.1	66.2±0.1	69.6±0.1
Tiny-ImageNet								
Clean acc.	59.1±0.4	45.5±0.2	46.3±0.4	34.3±7.8	54.9±0.2	60.4±0.1	51.3±0.3	56.0±0.2
mCA-N	23.6±0.5	28.7±0.1	28.0±0.5	23.7±5.8	25.8±1.1	30.5±1.3	37.5±0.1	39.6±0.6
Gaussian Noise*	22.0±0.6	29.7±0.1	28.6±0.6	23.9±6.1	25.3±0.9	28.8±1.3	38.0±0.2	39.9±0.7
Impulse Noise	23.0±0.3	25.4±0.1	25.2±0.5	23.2±4.6	23.8±1.5	29.8±1.4	35.5±0.1	38.7±0.5
Shot Noise	25.9±0.7	31.1±0.1	30.1±0.5	23.9±6.7	28.2±0.9	32.8±1.1	39.0±0.3	40.2±0.8

Table 1: Classification accuracy on clean CIFAR-10/CIFAR-100/Tiny-ImageNet datasets and Mean Corrupted Accuracy (mCA-N) on noise corruption subsets of CIFAR-10-C/CIFAR-100-C/Tiny-ImageNet-C datasets for ResNet-18 architecture. DiGN achieves the highest mCA-N score across all baselines. *The 'gaussian noise' corruption was excluded in the computation of mCA-N and is included here for completeness.

	Standard	AT	TRADES	RSE	DeepAugment	AugMix	DiGNw.o.CR	DiGN
CIFAR-10								
Clean RMSE	5.5±0.2	4.5±1.3	18.7±0.4	6.3±1.0	4.3±0.3	1.5±0.3	6.5±0.2	5.2±0.4
Corrupt RMSE-N	30.4±1.7	2.2±1.0	16.7±0.5	9.7±0.6	7.7±0.1	6.5±0.3	7.2±0.2	5.6±0.2
CIFAR-100								
Clean RMSE	8.5±0.1	5.2±2.3	4.0±1.2	12.9±0.5	10.2±0.1	2.8±0.4	11.9±0.1	6.5±0.3
Corrupt RMSE-N	34.1±0.8	6.9±2.1	2.6±0.9	17.4±0.6	15.7±0.1	17.4±0.9	12.3±0.2	9.0±0.2
Tiny-ImageNet								
Clean RMSE	10.3±0.1	8.2±0.3	10.4±0.3	18.0±0.6	7.6±0.8	4.6±0.6	10.6±0.1	9.7±1.1
Corrupt RMSE-N	28.9±0.3	2.2±0.4	3.6±0.2	24.1±0.4	19.4±0.6	23.6±8.3	16.2±0.4	15.5±0.8

Table 2: RMS calibration error on clean CIFAR-10/CIFAR-100/Tiny-ImageNet datasets and noise corruption subsets (excluding 'gaussian noise') of CIFAR-10-C/CIFAR-100-C/Tiny-ImageNet-C datasets for ResNet-18 architecture. DiGN achieves a significant reduction in corrupt RMSE-N over Standard and AugMix training.

	Standard	AugMix	DiGN	DiGN +AugMix
CIFAR-10				
mCA	77.7±0.3	89.3±0.1	86.3±0.2	90.7±0.1
Clean RMSE	5.5±0.2	1.5±0.3	5.2±0.4	2.2±0.3
Corrupt RMSE	17.1±0.2	3.1±0.3	9.5±0.3	1.0±0.2
CIFAR-100				
mCA	51.1±0.1	64.8±0.3	62.1±0.1	67.8±0.1
Clean RMSE	8.5±0.1	2.8±0.3	6.5±0.3	2.8±0.1
Corrupt RMSE	20.1±0.3	9.8±0.6	10.1±0.4	2.7±0.2
Tiny-ImageNet				
mCA	25.5±0.2	36.0±0.6	28.5±1.0	36.6±0.2
Clean RMSE	10.3±0.1	4.6±0.6	9.7±1.1	6.4±1.5
Corrupt RMSE	25.1±0.2	15.3±6.5	19.8±1.6	4.7±2.6

Table 3: Robustness and RMS calibration error on all common corruptions on ResNet-18 architecture. DiGN improves upon Standard training considerably, and in combination with AugMix achieves highest mCA score and lowest RMSE on common corruptions.

method yields state-of-the-art robustness and uncertainty calibration under unforeseen noise domain shifts, for different network architectures and datasets. In addition, our approach in combination with diverse data augmentations provides state-of-the-art robustness and uncertainty calibration under unforeseen common corruptions.

	Standard	AugMix	DiGN	DiGN +AugMix
CIFAR-10				
DenseNet-121				
Clean acc.	93.9±0.1	94.6±0.1	93.0±0.1	94.4±0.0
mCA-N	56.1±1.8	80.7±0.9	90.0±0.2	90.7±0.1
mCA	75.2±0.3	87.9±0.2	85.1±0.2	90.0±0.1
Wide-ResNet-18				
Clean acc.	94.5±0.2	95.5±0.3	94.3±0.0	95.9±0.1
mCA-N	59.1±1.7	84.5±0.4	91.9±0.3	92.5±0.1
mCA	78.9±0.6	90.0±0.2	87.7±0.3	92.1±0.1
CIFAR-100				
DenseNet-121				
Clean acc.	74.2±0.2	76.2±0.1	71.6±0.1	75.6±0.3
mCA-N	26.3±0.4	52.9±0.1	65.9±0.1	67.9±0.2
mCA	47.6±0.5	63.2±0.2	59.2±0.1	66.6±0.3
Wide-ResNet-18				
Clean acc.	75.3±0.6	77.0±0.5	75.3±0.4	77.6±0.2
mCA-N	37.4±2.8	56.7±0.6	70.7±0.3	71.7±0.2
mCA	55.1±0.6	65.9±0.5	64.7±0.5	69.6±0.3

Table 4: Robustness on noise and all common corruptions on DenseNet-121 and Wide ResNet-18 architectures. DiGN improves upon Standard training considerably, and in combination with AugMix achieves highest mCA score on digital noise and all common corruptions.

References

- A. Krizhevsky, I. Sutskever, and G. E. Hinton. Imagenet classification with deep convolutional neural networks. In *Advances in Neural Information Processing Systems*, 2012.
- K. He, X. Zhang, S. Ren, and J. Sun. Delving deep into rectifiers: Surpassing human-level performance on imagenet classification. In *ICCV*, 2015.
- Yanping Huang, Youlong Cheng, Ankur Bapna, Orhan Firat, Mia Xu Chen, Dehao Chen, HyukJoong Lee, Jiquan Ngiam, Quoc V. Le, Yonghui Wu, and Zhifeng Chen. Gpipe: Efficient training of giant neural networks using pipeline parallelism. In *NeurIPS*, 2019.
- Dan Hendrycks and Thomas Dietterich. Benchmarking neural network robustness to common corruptions and perturbations. In *ICLR*, 2019.
- L. Engstrom, B. Tran, D. Tsipras, L. Schmidt, and A. Madry. Exploring the landscape of spatial robustness. In *ICML*, 2019.
- A. Torralba and A. A. Efros. Unbiased look at dataset bias. In *CVPR*, 2011.
- B. Recht, R. Roelofs, L. Schmidt, and V. Shankar. Unbiased look at dataset bias. In *ICML*, 2019.
- A. Madry, A. Makelov, L. Schmidt, D. Tsipras, and A. Vladu. Towards deep learning models resistant to adversarial attacks. In *ICLR*, 2018.
- H. Zhang, Y. Yu, J. Jiao, E. P. Xing, L. El Ghaoui, and M. I. Jordan. Theoretically principled trade-off between robustness and accuracy. In *ICML*, 2019.
- A. Joshi, A. Mukherjee, S. Sarkar, and C. Hegde. Semantic adversarial attacks: Parametric transformations that fool deep classifiers. In *ICCV*, 2019.
- K. Xiao, L. Engstrom, A. Ilyas, and A. Madry. Noise or signal: The role of image backgrounds in object recognition. In *ICLR*, 2021.
- D. Kang, Y. Sun, D. Hendrycks, T. Brown, and J. Steinhardt. Testing robustness against unforeseen adversaries. In *arXiv pre-print arxiv:1908.08016*, 2019.
- R. Geirhos, C. R. M. Temme, J. Rauber, H. H. Schutt, M. Bethge, and F. A. Wichmann. Generalisation in humans and deep neural networks. In *NeurIPS*, 2018.
- S. Chun, S. J. Oh, S. Yun, D. Han, J. Choe, and Y. Yoo. An empirical evaluation on robustness and uncertainty of regularization methods. In *ICML Workshop on Uncertainty and Robustness in Deep Learning*, 2019.
- E. D. Cubuk, B. Zoph, D. Mane, V. Vasudevan, and Q. V. Le. Autoaugment: Learning augmentation strategies from data. In *CVPR*, 2019.
- Balaji Lakshminarayanan, Alexander Pritzel, and Charles Blundell. Simple and scalable predictive uncertainty estimation using deep ensembles. In *NeurIPS*, 2017.
- Dan Hendrycks, Kimin Lee, and Mantas Mazeika. Using pre-training can improve model robustness and uncertainty. In *ICML*, 2019.
- Yaniv Ovadia, Emily Fertig, Jie Ren, Zachary Nado D Sculley, Sebastian Nowozin, Joshua V Dillon, Balaji Lakshminarayanan, and Jasper Snoek. Can you trust your model’s uncertainty? evaluating predictive uncertainty under dataset shift. In *NeurIPS*, 2019.
- D. Hendrycks, N. Mu, E. D. Cubuk, B. Zoph, J. Gilmer, and B. Lakshminarayanan. Augmix: A simple data processing method to improve robustness and uncertainty. In *ICLR*, 2020.
- D. Hendrycks, S. Basart, N. Mu, et al. The many faces of robustness: A critical analysis of out-of-distribution generalization. In *ICCV*, 2021.
- R. C. Gonzalez and R. E. Woods. *Digital Image Processing*. Pearson, 2018.
- A. Awad. Denoising images corrupted with impulse, gaussian, or a mixture of impulse and gaussian noise. *Engineering Science and Technology, an International Journal*, 22(3), 2019.
- Dimitris Tsipras, Shibani Santurkar, Logan Engstrom, Alexander Turner, and Aleksander Madry. Robustness may be at odds with accuracy. In *ICLR*, 2019.
- X. Liu, M. Cheng, H. Zhang, and C.-J. Hsieh. Towards robust neural networks via random self-ensemble. In *ECCV*, 2018.
- T. DeVries and G. W. Taylor. Improved regularization of convolutional neural networks with cutout. In *arXiv:1708.04552*, 2017.
- Hongyi Zhang, Moustapha Cisse, Yann Dauphin, and David Lopez-Paz. mixup: Beyond empirical risk minimization. In *ICLR*, 2017.
- Yuji Tokozume, Yoshitaka Ushiku, and Tatsuya Harada. Between-class learning for image classification. In *CVPR*, 2018.
- Sangdoo Yun, Dongyoon Han, Seong Joon Oh, Sanghyuk Chun, Junsuk Choe, and Youngjoon Yoo. Cutmix: Regularization strategy to train strong classifiers with localizable features. In *ICCV*, 2019.
- Ekin Dogus Cubuk, Barret Zoph, Dandelion Mane, Vijay Vasudevan, and Quoc V. Le. Autoaugment: learning augmentation policies from data. In *CVPR*, 2018.
- S. Kullback. *Information Theory and Statistics*. Dover, 1997.
- Alex Krizhevsky, Vinod Nair, and Geoffrey Hinton. Cifar-10 and cifar-100 datasets, 2009. URL <https://www.cs.toronto.edu/~kriz/cifar.html>.
- Fei-Fei Li, Andrej Karpathy, and Justin Johnson. Tiny imagenet dataset - cs231n course stanford, 2014. URL <http://cs231n.stanford.edu/tiny-imagenet-200.zip>.
- K. He, X. Zhang, S. Ren, and J. Sun. Deep residual learning for image recognition. In *CVPR*, 2016.
- Gao Huang, Zhuang Liu, Laurens van der Maaten, and Kilian Q Weinberger. Densely connected convolutional networks. In *CVPR*, 2017.
- C. Lin, J. Martens, S. Goyal, D. Krishnan, K. Dvijotham, A. Fawzi, S. De, R. Stanforth, and P. Kohli. Adversarial robustness through local linearization. In *NeurIPS*, 2019.

7 Supplementary Material

7.1 Data Corruption Visualizations

An example image along with its corrupted versions is shown in Figure 2; although humans might be able to recognize this as a boat, a deep learning image classifier trained in a standard manner will fail against most of these corruptions.

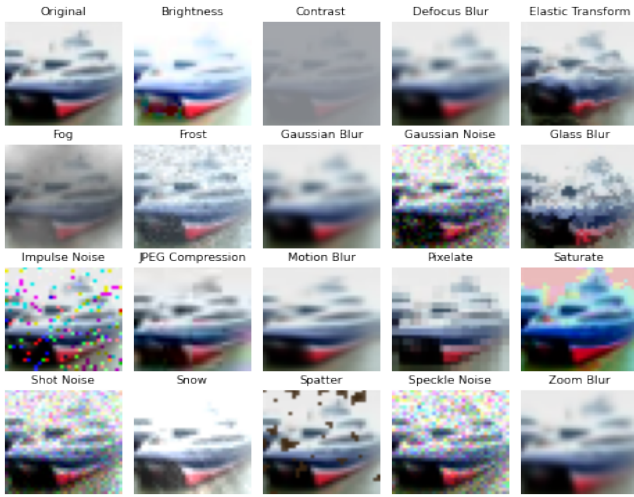


Figure 2: Example CIFAR-10 test image along with its corrupted versions. These corruptions are not available in the training process, and are only used for evaluation at inference time.

7.2 Proof of Proposition 1

Proof: From Appendix C in [Lin et al., 2019], the Hessian of the softmax cross-entropy function can be decomposed as:

$$H(x) = J^T(\text{diag}(p) - pp^T)J$$

where J denotes the Jacobian of the network function f_θ (logits) and p denotes the softmax probabilities. The Jacobian transposed is denoted as $J^T = [J_1^T, \dots, J_K^T]$ with $J_k :=$

$\nabla_x f_k(x)^T$. Starting from the FIM in (7), we have:

$$\begin{aligned} G_\theta(x) &= \sum_k p_k (\nabla_x \log p_k) (\nabla_x \log p_k)^T \\ &= \sum_k p_k (\nabla_x f_k - J^T p) (\nabla_x f_k - J^T p)^T \\ &= \sum_k p_k (\nabla_x f_k \nabla_x f_k^T - \nabla_x f_k p^T J \\ &\quad - J^T p \nabla_x f_k^T + J^T p p^T J) \\ &= \sum_k p_k \nabla_x f_k \nabla_x f_k^T - \left(\sum_k p_k \nabla_x f_k \right) p^T J \\ &\quad - J^T p \left(\sum_k p_k \nabla_x f_k \right)^T + J^T p p^T J \\ &= \sum_k p_k \nabla_x f_k \nabla_x f_k^T - J^T p p^T J \\ &\quad - J^T p p^T J + J^T p p^T J \\ &= \sum_k p_k J_k^T J_k - J^T p p^T J \\ &= J^T \text{diag}(p) J - J^T p p^T J \\ &= J^T (\text{diag}(p) - p p^T) J \\ &= H(x) \end{aligned}$$

This concludes the proof. \square

7.3 Proof of Theorem 1

Proof: Using the quadratic loss approximation near x , we have:

$$\mathcal{L}(x + \delta, y) = \mathcal{L}(x, y) + \delta^T \nabla_x \mathcal{L}(x, y) + \frac{1}{2} \delta^T H(x) \delta + o(\|\delta\|_2^2)$$

By using up to second order terms, an upper bound on the loss variation holds as:

$$\begin{aligned} |\mathcal{L}(x + \delta, y) - \mathcal{L}(x, y)| &\approx |\langle \nabla_x \mathcal{L}(x, y), \delta \rangle + \frac{1}{2} \delta^T H(x) \delta| \\ &\leq \|\delta\|_2 \cdot \|\nabla_x \mathcal{L}(x, y)\|_2 + \frac{1}{2} \delta^T H(x) \delta \quad (13) \end{aligned}$$

where we used the triangle inequality, and the Cauchy-Schwarz inequality to bound the linear term and the fact that $H(x)$ is positive semidefinite. The gradient in the first term of (13) can be written as:

$$\begin{aligned} \|\nabla_x \mathcal{L}(x, y)\|_2 &= \sqrt{\left\| \sum_k -y_k \nabla_x \log p(x)_k \right\|_2^2} = \sqrt{\sum_k y_k \|\nabla_x \log p(x)_k\|_2^2} \\ &= \sqrt{\sum_k e_k \|\nabla_x \log p(x)_k\|_2^2 + \sum_k p(x)_k \|\nabla_x \log p(x)_k\|_2^2} \end{aligned}$$

where $e_k = y_k - p(x)_k$ is the prediction error. The quadratic form in (13) can be upper bounded using the eigenvalue bound:

$$\delta^T H(x) \delta \leq \lambda_{\max}(H(x)) \|\delta\|_2^2$$

Using the two preceding bounds into (13), the desired bound (11) is obtained. The proof is complete. \square

7.4 Experimental Results

Robustness and Calibration Performance across Network Architectures. Table 5 shows the robustness and calibration metrics for CIFAR-10/100 datasets of popular baselines and our proposed DiGN method on the DenseNet-121 and Wide-ResNet-18 architectures. The ResNet-18 architecture consists of layers with widths 64, 128, 256, 512, and the Wide-ResNet-18 architecture uses widths 320, 640, 1280, 2560 instead.

The results presented for ResNet-18 generalize to other architectures; the hybrid combination DiGN + AugMix (a) achieves the highest mCA-N and mCA scores without sacrificing clean accuracy, and (b) reaches low RMSE-N and RMSE scores with good clean RMSE performance.

	Standard	AugMix	DiGN	DiGN + AugMix
CIFAR-10				
DenseNet-121				
Clean acc.	93.9±0.1	94.6±0.1	93.0±0.1	94.4±0.0
mCA-N	56.1±1.8	80.7±0.9	90.0±0.2	90.7±0.1
mCA	75.2±0.3	87.9±0.2	85.1±0.2	90.0±0.1
Clean RMSE	6.3±0.0	3.3±0.1	5.9±0.2	4.8±0.4
Corrupt RMSE-N	32.6±1.9	6.6±0.2	6.5±0.4	2.5±0.4
Corrupt RMSE	20.7±0.3	2.5±0.0	10.6±0.0	2.6±0.2
Wide-ResNet-18				
Clean acc.	94.5±0.2	95.5±0.3	94.3±0.0	95.9±0.1
mCA-N	59.1±1.7	84.5±0.4	91.9±0.3	92.5±0.1
mCA	78.9±0.6	90.0±0.2	87.7±0.3	92.1±0.1
Clean RMSE	4.91±0.0	1.9±0.2	4.3±0.5	2.0±0.2
Corrupt RMSE-N	29.0±1.2	8.7±0.5	5.2±0.2	3.4±0.3
Corrupt RMSE	16.1±0.5	5.1±0.5	8.1±0.5	3.6±0.5
CIFAR-100				
DenseNet-121				
Clean acc.	74.2±0.2	76.2±0.1	71.6±0.1	75.6±0.3
mCA-N	26.3±0.4	52.9±0.1	65.9±0.1	67.9±0.2
mCA	47.6±0.5	63.2±0.2	59.2±0.1	66.6±0.3
Clean RMSE	12.6±1.9	4.6±0.1	13.8±0.1	9.4±0.2
Corrupt RMSE-N	43.5±2.4	7.8±0.4	14.1±0.3	5.6±0.4
Corrupt RMSE	28.6±2.6	2.7±0.1	19.2±0.3	5.5±0.3
Wide-ResNet-18				
Clean acc.	75.3±0.6	77.0±0.5	75.3±0.4	77.6±0.2
mCA-N	37.4±2.8	56.7±0.6	70.7±0.3	71.7±0.2
mCA	55.1±0.6	65.9±0.5	64.7±0.5	69.6±0.3
Clean RMSE	5.2±0.1	3.6±0.5	6.1±0.3	3.3±0.6
Corrupt RMSE-N	21.6±2.2	20.8±0.3	4.1±0.0	8.9±0.3
Corrupt RMSE	11.7±0.6	10.1±0.3	4.7±0.2	4.6±0.2

Table 5: Robustness and RMS calibration error on noise and all common corruptions on DenseNet-121 and Wide ResNet-18 architectures. DiGN improves upon Standard training considerably, and in combination with AugMix achieves highest mCA score and lowest RMSE on common corruptions.

Hyperparameter Sensitivity. We study the effect of the training hyperparameters ($\lambda, \sigma_{\max}, n$) on the robustness performance of DiGN training using the ResNet-18 architecture for CIFAR-10 and CIFAR-100 datasets.

Table 6 contains the clean accuracy, mean corrupted accuracy over noise (mCA-N) and all corruptions (mCA). It is evident that the robustness performance is not too sensitive to the choice of hyperparameters.

$\lambda, \sigma_{\max}, n$	Clean accuracy	mCA-N	mCA
CIFAR-10			
0.5, 0.2, 3	92.8±0.2	90.6±0.1	85.8±0.1
0.4, 0.2, 3	93.2±0.1	90.5±0.3	85.8±0.4
0.3, 0.2, 3	93.0±0.1	90.7±0.1	86.1±0.3
0.2, 0.2, 3	93.6±0.1	91.0±0.1	86.3±0.2
0.4, 0.2, 1	92.9±0.1	90.6±0.2	85.9±0.1
0.3, 0.2, 1	93.4±0.1	90.5±0.3	85.9±0.5
0.2, 0.2, 1	93.3±0.2	90.2±0.4	85.9±0.1
0.1, 0.2, 1	93.6±0.1	89.8±0.2	85.1±0.3
0.05, 0.2, 1	93.5±0.1	89.1±0.2	84.6±0.3
0.02, 0.2, 1	93.3±0.1	87.5±0.2	83.4±0.4
0.02, 0.3, 1	92.9±0.2	87.2±0.4	82.5±0.6
CIFAR-100			
0.4, 0.2, 3	72.1±0.1	68.2±0.3	61.8±0.2
0.3, 0.2, 3	72.8±0.1	68.5±0.1	62.1±0.1
0.2, 0.2, 3	73.1±0.1	68.2±0.4	62.0±0.4
0.05, 0.2, 1	74.4±0.1	65.4±0.1	60.2±0.1
0.02, 0.2, 1	74.4±0.1	62.2±0.1	58.7±0.2
0.02, 0.3, 1	73.3±0.3	62.0±0.3	58.4±0.3
0.3, 0.2, 1	73.0±0.2	67.9±0.3	61.7±0.1
0.2, 0.2, 1	73.3±0.1	67.7±0.3	61.4±0.2
0.1, 0.2, 1	74.2±0.2	67.1±0.2	60.8±0.3

Table 6: Sensitivity analysis on hyperparameters of our DiGN training method. Test set accuracy for CIFAR-10/100 and CIFAR-10/100-C datasets on ResNet-18 architecture are shown.